MESOSCALE VARIABILITIES IN SEA SURFACE CURRENT FIELDS DERIVED THROUGH MULTI-SENSOR TRACKING OF SEA SURFACE FILMS

Benjamin Seppke [(1)], Martin Gade [(2)], Leonie Dreschler-Fischer [(2)]

[(1)] University of Hamburg, Department of Informatics, Email: {seppke,dreschler}@informatik.uni-hamburg.de
[(2)] University of Hamburg, Institute of Oceanography, Email: martin.gade@uni-hamburg.de

ABSTRACT

In recent studies [1], we have already shown that it is possible to derive mesoscale sea surface current fields by tracking signatures of marine surface films in multi-sensor satellite data. Although the derived sea surface current fields corresponded well with those provided by numerical models, the former mainly showed large-scale current properties. This is insofar remarkable, as the traced signatures clearly follow local dynamical features such as eddies or dipoles. In this paper, we present a new approach, which allows to extract, and even overemphasize, the affine local current component for the derived current fields [2]. Depending on the spatial resolution of the derived current fields this method allows a deeper insight into the turbulent nature of those fields. As a result, the imaged signatures can be seen as local variabilities of sea surface currents of larger scales. Moreover, these local variabilities seem to be mainly independent of the 'global' currents.

1. INTRODUCTION

The investigation of mesoscale turbulent sea surface currents is of high interdisciplinary interest, since it results in a better understanding of ocean-atmosphere interactions and may help to improve numerical model results, particularly in coastal waters.

In this work, we present recent results of sea surface current fields derived from multi-sensor satellite imagery. The sea surface currents were derived by means of tracking biogenic marine surface films within satellite image series. Massive algae blooms cause the accumulation of these surface films in many different waters and coastal areas. In two case studies, we will first demonstrate the results for the Northern Baltic Sea and the Southern California Bight.

In [1] we have also shown that the derived sea surface current fields corresponded well with those provided by numerical models, the former mainly showed large-scale current properties. This is insofar remarkable, as the traced signatures clearly follow local dynamical features such as eddies or dipoles.

To further investigate this, we present a newly developed approach, which allows to extract and even overemphasize the affine local current component for the derived current fields [2].

Depending on the spatial resolution of the derived current fields this method allows a deeper insight into the turbulent nature of those fields at meso- and sub-mesoscale [3]. First results of the application of our method will be presented for sea surface currents, which have been derived using SAR- and multispectral imagery.

2. REGIONS OF INTEREST

Since two different regions of interest (ROIs) are used in this paper to demonstrate the current field decomposition, we distinguish these both regions in the following subsections. Details regarding the derivation of the sea surface current fields for both regions can be found in [2].

2.1. Northern Baltic Sea

The first investigated area is the Northern Baltic Proper, north of the Swedish island of Gotland. On July 15, 1997, a day with extensive cyanobacterial blooms in the northern Baltic Proper, data from three different satellite sensors were acquired over the same area, including the Thematic Mapper (TM) aboard Landsat, the Synthetic Aperture Radar (SAR) aboard ERS-2 and the Wide-Field Scanner (WiFS) aboard IRS-1C. Fig. 1 shows a map of the first ROI in which the satellite coverage is highlighted for each sensor.

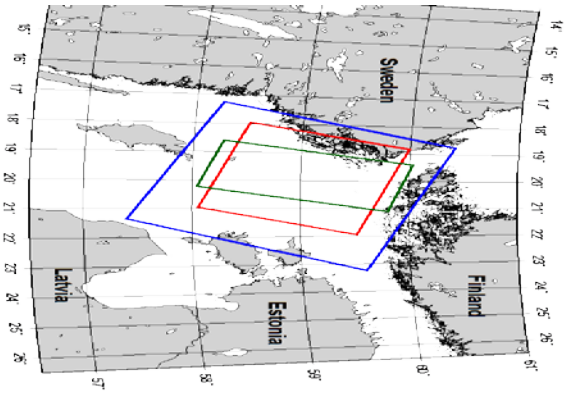

Figure 1. Map of the Northern Baltic Sea (Baltic Proper) indicating the location of the satellite images used for the first study presented herein at July 15, 1997: ERS-2 SAR (green), Landsat TM (red) and IRS WiFS (dark blue). Image source: [2].

The high morpo-dynamic of the biogenic surface films requires a small time gap between the acquisitions. At the first region, the three satellite sensors image the area within less than two hours. All sensors provide a spatial resolution of at least 188 m per pixel, which makes mesoscale surface current features detectable. The exact satellite characteristics of each acquisition can be found in tab. 1.

Table 1. Satellite characteristics for the first case. The date of all acquisitions is July 15, 1997.

Platform	Sensor	Resolution (m)	Time (UTC)
Landsat 5	TM	30.0	08:57
ERS-2	SAR	12.5	09:47
IRS-1C	WiFS	188.0	10:26

Due to an extensive algae bloom, signatures of accumulated algae are visible on all acquired images, like as brighter linear structures in most parts of the (multispectral) Landsat TM image (fig. 2). For further analysis, we have selected a central ROI, which has been imaged by all three sensors. This region is shown in fig. 2 superimposed on the false-color Landsat TM image. Fig. 2 also shows a lot of vortical structures of surface films:

1. A dipole at the upper left area,
2. An eddy at the lower area.

The correspondence between these signatures and the local sea surface current turbulences will be discussed later. To focus on the detection of mesoscale variabilites, we only use the derived current fields of the SAR-WiFS image pair, because there is nearly no cloud coverage affecting this pair.

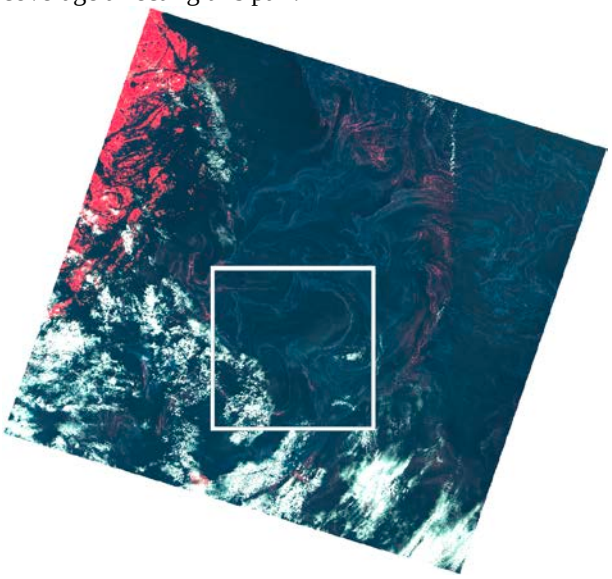

Figure 2. False colour representation of the Landsat TM image acquired at July 15, 1997: The white square denotes the first ROI. Brighter linear signatures refer to sea surface films and white signatures denote clouds.

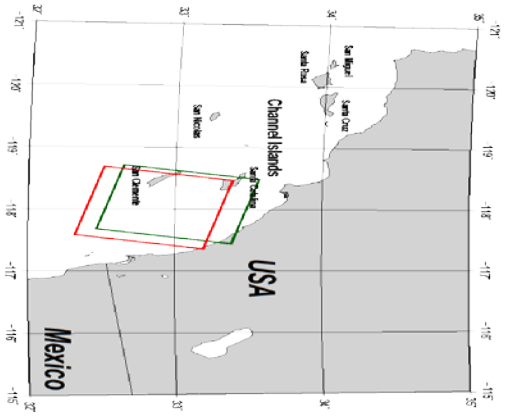

Figure 3. Map of the Southern California Bight indicating the location of the satellite images used for the second case study presented herein at September 27, 2003: ENVISAT ASAR (green) and ERS-2 SAR (red). Image source: [2].

2.2. Southern California Bight

Unlike the first ROI, where multispectral and SAR images have been used to derive the sea surface currents, two different SAR images will be used for the Southern California Bight. Both, the ENVISAT ASAR and the ERS-2 SAR sensor, imaged the area of interest within less than half an hour. The satellite coverage is depicted by means of a map in fig. 3.
Both SAR sensors are capable of a comparably high-resolution acquisition of 12.5x12.5 m^2 per pixel. Further details can be found in tab. 2. In contrast to the first region, this image resolution allows the derivation of a high-resolution surface current field.

Table 2. Satellite characteristics for the second case. The date of all acquisitions is September 27, 2003.

Platform	Sensor	Resolution (m)	Time (UTC)
ENVISAT	ASAR	12.5	18:01
ERS-2	SAR	12.5	18:30

During the acquisitions, there was a northern wind with speeds of about 2.1 m/s measured on the island of San Clemente. Due to the relatively high and non-uniform turbulent wind, the signatures on both SAR images look rather noisy and inhomogeneous. As an example, the ENVISAT acquisition is shown in fig. 4. There are, however, a few regions with rather high and constant normalized radar backscatter. This is caused by the high roughness of the sea surface in these areas. The reason for this is the coherent coupling of small-scale waves, which are wind-induced.
In the ROI of the second area, which is highlighted in fig. 4, we can observe linear signatures of lower radar backscatter. Biogenic marine surface films cause a dampening the small scale waves, thus these signatures correspond to sea surface films produced e.g. by algae blooms [4].

Figure 4. The second investigated region. The ROI is depicted by a white square. The contrast enhanced ENVISAT ASAR image is shown in the background.

3. METHODS

In [2], we have presented a framework, which makes the well-known and theoretically proven motion-detection algorithms applicable to the application domain of deriving sea surface currents by tracking sea surfaces film at satellite images of different sensors and sensor modalities. The large spatio-temporal distance between the tracers has been one main challenge in the design of this framework, since it results in large search spaces for the class of feature-based approaches and may even yield to a vanishing congruence between the image series' gradients and the Optical Flow Constraint Equation (OFCE).

To cope this, in [1] we propose the use of a technique, which is able to estimate the global displacement of the overall movement based on an adapted algorithm, which has been described by Y. Sun in [5].

Let us assume that a global motion model exists, which describes the global part of a derived sea surface current field:

1. Let $(x, y, u, v)^T \in VF$ be the components of the current field, where $(x, y)^T$ is the position and $(u, v)^T$ the direction of each vector in VF, and let M be a affine matrix containing the global motion component.
2. The global part of each $(x, y, u, v)^T \in VF$ is given by a matrix multiplication of each position vector with the model:

$$(x_g, y_g, 1)^T = M \cdot (x, y, 1)^T \quad (1)$$

Using the results of eq. 1, the global displacement can be described as:

$$(u_g, v_g)^T = (x_g - x, y_g - y) \quad (2)$$

for each displacement vector.

3. The local part of the motion can now easily be derived using the global displacement of eq. 2:

$$(u_l, v_l)^T = (u - u_g, v - v_g) \quad (3)$$

To overemphasize the local component, each local displacement of eq. 3 may be scaled by a constant factor or to a given fixed length.

Based on the results of each algorithm inside the framework described above, we propose two possibilities to compute the (global) affine matrix M of the sea surface current field.

3.1. Using the global motion estimation

During the computation of the global motion, an affine transformation has already been computed. If this matrix, which encodes rotation in translation in this case, is saved in conjunction with the current field, no further post processing or computation is needed.

3.2. Estimate affine matrix from current field

If the sea surface current field has been derived without the global motion estimation, no affine matrix has yet been be assigned to it. In this case we propose the use of a minimum mean square error estimation of the affine matrix of the sea surface current field.

The rationale behind this approach is to consider the current field as a set of point correspondences. Based on these correspondences, finding an affine matrix can be redefined as finding an affine registration between all of the correspondences [6]:

1. Let $(x, y, u, v)^T \in VF$ be the components of the current field, where $(x, y)^T$ is the position and $(u, v)^T$ the direction of each vector in VF.
2. Define two sets P_1 and P_2, to separate the elements of VF. For each $(x, y, u, v)^T \in VF$:
   a. Put $(x, y, 1)^T$ into P_1 and
   b. Put $(x + u, y + v, 1)^T$ into P_2.
3. For all $\overrightarrow{p_1}$ in P_1 and $\overrightarrow{p_2}$ in P_2 in conjunction, pose and solve the following system of linear equations:

$$\begin{pmatrix} a_{11} & a_{12} & a_{13} \\ a_{21} & a_{22} & a_{23} \\ 0 & 0 & 1 \end{pmatrix} \cdot \overrightarrow{p_1} = \overrightarrow{p_2} \quad (4)$$

Since there are six unknowns in Eq. 4, we need at least three point correspondences to compute the affine component of the sea surface current field. With three points, however, the global motion is equal to the complete displacement and the local motion vanishes.

Only if more than three correspondences are used, the local component will become evident by means of the square error of each vector with respect to the approximation described by the global model. After approximation, the affine matrix M exists and can be used for overemphasized local current component visualization as described above.

3.3. DISCUSSION

In [1] and [2] we have already described the approaches to derive current fields from multi-sensor satellite imagery. In this discussion, we will skip the derivation part and present the global/local decomposition based on derived current fields for both ROIs.

3.4. Northern Baltic Sea

Before we start with the decomposition for the first area, we present the ROI and the derived current field in detail. Fig. 5 shows the image data of this region, where turbulent signatures of accumulated surface films have been highlighted. Fig. 6(a) shows the derived sea surface current field. For the derivation the fast normalized cross-correlation between features, which have been detected for the ERS-2 SAR and the IRS WiFS acquisition [7]. In the derived results, one cannot see any dependency between the turbulent signatures and the behaviour of the current field.
If we use the technique presented in sec. 3.2 to estimate the local motion part and overemphasize this part, we will get a much better explanation the those structures. Fig. 6(b) shows this by strong correspondences between the local sea surface currents.
This local correspondence is insofar, as a smoothness assignment of features has been used to generate it. Even after this smoothing step, the local current dynamics follows the signatures.
This is the first time that such an explanation for the eddy and dipole dynamic in a larger flow field has been discovered by the use of multi-sensor satellite imagery.

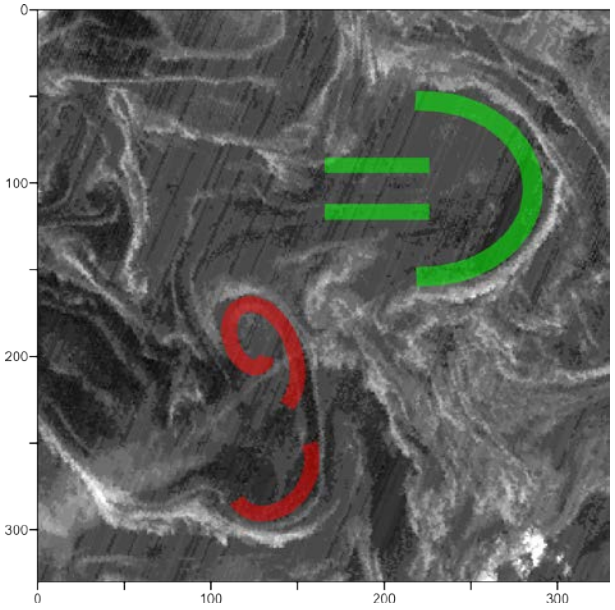

Figure 5: The ROI of first region as imaged by the WiFS sensor (near infrared, band 4). The surface films accumulate according to a dipole (green) and one complete and one incomplete eddy (red).

Additionally, from fig. 6(b) we derive can the eddy and its neighboured half-eddy may form a new dipole in future. The local sea surface current component gives strong evidence as it already defines a dipole flow field instead of two uncoupled eddies.

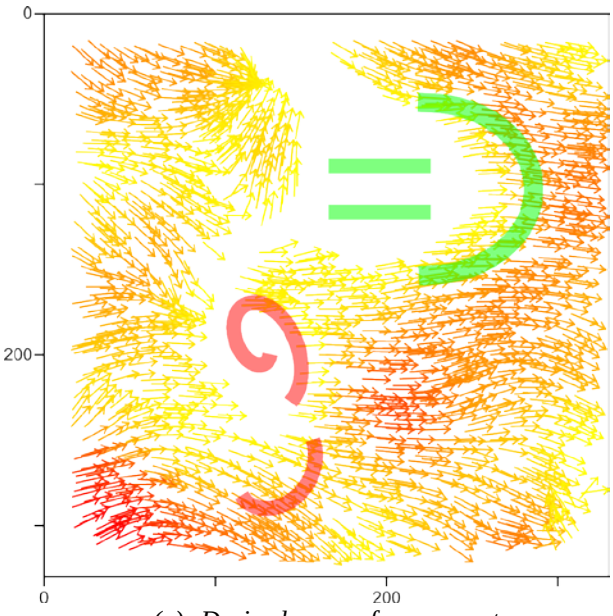

(a) Derived sea surface currents

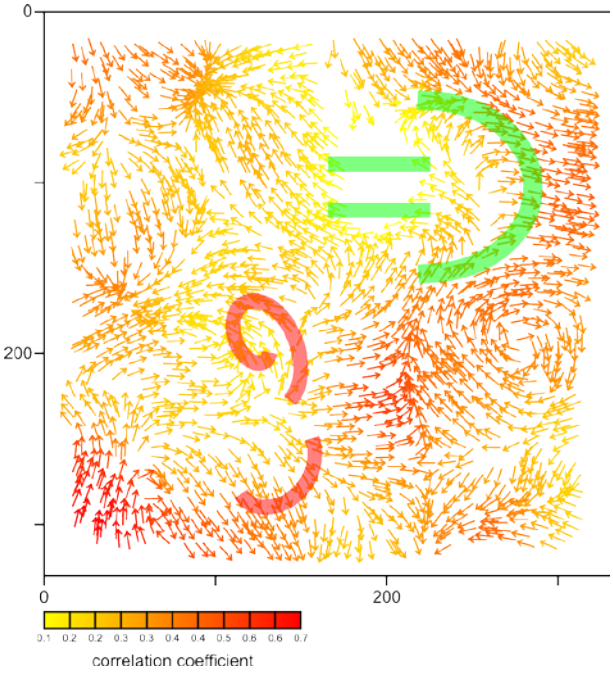

(b) Overemphasized local motion component

Figure 6: Comparison of the derived sea surface currents with the result of the local motion extraction on the overemphasized representation for the first ROI (Baltic Sea). Like in fig. 5, the dipole and eddies are overlaid in red and green.

3.5. Southern California Bight

The second region differs from the first one in a variety of aspects. First of all, we have a different image setup with two comparable image sources, which allows the use of either feature- or gradient-based motion detection algorithms. In addition, the image resolution is about ten times higher compared to the first ROI. This makes it possible to even monitor small-scale surface current properties. Due to the image characteristics, the global motion detection could be performed for this region.

Fig. 7 shows the ROI for this region, which contains two interesting turbulent signatures: an eddy and a morphed (degraded) dipole. In contrast to these signatures, all derived current fields show an uninfluenced constant current in direction to the coast (North East) [2]. This refers to a large amount of the so-called global motion, and a potentially very small amount of local sea surface current variability.

Since the global motion estimation has been used to derive the current fields, we will use the affine matrix of this approach for the vector field decomposition. The results of the decomposition are given in detail for both interesting signatures and for the feature- and gradient-based approach in fig. 8.

The detailed view on the local surface current of the eddy signature in fig. 8(a) unveils that beyond the global current, there is a significant local current property, which can be used to explain the eddy signature depicted in fig. 7.

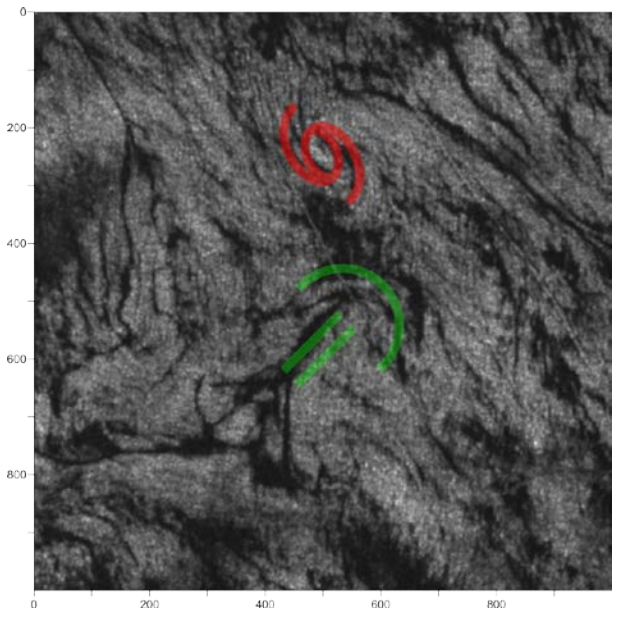

Figure 7: The ROI of second region as imaged by the ENVISAT ASAR. The image has been Gamma-MAP filtered to reduce speckle-noise [8]. The surface films (darker linear signatures) accumulate to a dipole (green) and one eddy (red). The size of the image area is 12,5x12.5 km^2.

Due to the large global current part, this surface current variability was hidden before the decomposition and overemphasizing of the local component.

Another mentionable fact is that the turbulent behaviour of the eddy signature could be observed by our method, although the corresponding signature is of a small size of only about 2x2 km^2. This demonstrates that the proposed decomposition can also be used to explain structures far below the mesoscale.

In contrast to the interpretation of the local current component of the eddy, the analysis of the dipole's local current is more challenging (fig. 8(b)). Its local component shows only a small amount of the characteristic turbulences of a dipole. Moreover, an eddy-like behaviour can be observed, especially in the left image of fig 8(b), which has been derived using the feature-based approach. The reason for this unexpected local current pattern may be found in fig. 7. The dipole structure has already been degraded from a dipole to a kind of eddy-like structure. This restructuring process becomes visible in the local current component.

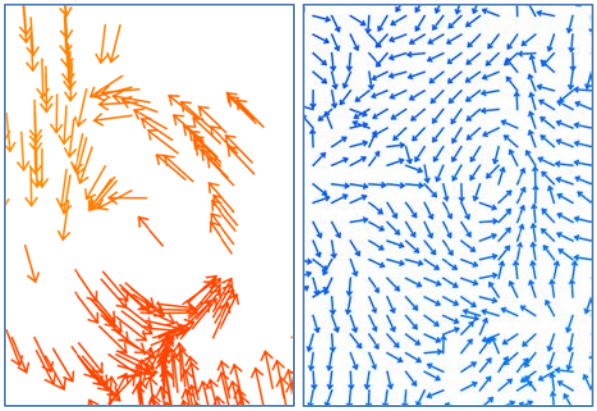

(a) Detailed view on the eddy signature

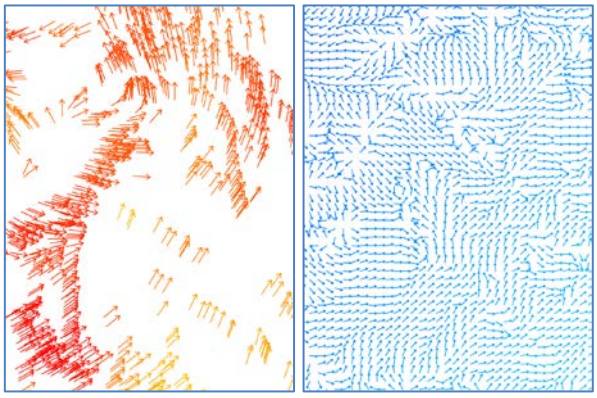

(b) Detailed view on the dipole signature

Figure 8: Detailed presentation of the overemphasized local sea surface current for the two signatures highlighted in fig. 7. Left: feature-based method (fast normalized cross-correlation), right: gradient-based Horn and Schunck approach [9].

4. CONCLUSIONS

We have presented a novel approach, which allows to extract and even overemphasize the local current component with respect to an affine global motion for sea surface current fields, which have been derived by tracking sea surface films using multi-sensor data. The approach is based on the decomposition of the derived current field into a local and a global motion part.

First results of the application of our method have been presented for sea surface currents, which have been derived using SAR- and multispectral imagery of the Baltic Sea and the Southern California Bight.

In contrast to the mostly large-scale ('global') currents, the results of the decomposition demonstrate that there is a strong correspondence between the eddy- and dipole-like signatures and the mesoscale and sub-mesoscale ('local') surface current components.

To conclude, the existence of specific imaged signatures of accumulated biogenic sea surface films can be explained by local variabilities of the sea surface currents of larger scales.

Moreover, these local variabilities seem to be mainly independent of the 'global' currents. Since the global motion part was much higher for the presented case studies, these meaningful local current variabilities were hidden before the decomposition.

Depending on the spatial resolution of the derived current fields this method allows a deeper insight into the turbulent nature of those fields. Using the approach presented herein, this is the first time that such turbulences can be monitored synoptically for such a large area at such a fine scale from space.

REFERENCES

1. Gade, M., Seppke, B. & Dreschler-Fischer, L. (2012), Mesoscale surface current fields in the Baltic Sea derived from multi-sensor satellite data, *International Journal of Remote Sensing* **33**(10), pp3122–3146.

2. Seppke, B. (2013), *Untersuchungen zum Korrespondenzproblem bei der Bestimmung mesoskaliger Strömungen der Meeresoberfläche anhand von Satellitenbildern*, Doctoral Thesis, University of Hamburg, Dept. of Informatics.

3. Seppke, B., Dreschler-Fischer, L. & Gade, M. (2012), Towards a tracking of small scale eddies using high-resolution RADARSAT-2 and TerraSAR-X imagery, *Proceedings of 1st EARSeL Workshop on Temporal Analysis of Satellite Images*

4. Gade,M., Alpers,M., Hühnerfuss, H., Masuko, H. & Kobayashi, T. (1998), The Imaging of Biogenic and Anthropogenic Surface Films by the Multi-frequency Multi-polarization SIR-C/X-SAR. *Journal of Geophysical Research* **103**(C9), pp18851–18866.

5. Sun, Y. (1996), Automatic Ice Motion Retrieval from ERS-1 SAR Images Using The Optical Flow Method, *International Journal of Remote Sensing* **17**(11), pp2059–2087

6. Brown, L. G. (1992). A survey of image registration techniques. *ACM Comput. Surv.* **24**, pp325–376.

7. Lewis, J. P. (1995), Fast Template Matching, *Vision Interface '95*, pp15–19.

8. Lopes, A., Nezry, E., Touz, R. & Laur, H. (1990), Maximum a posteriori speckle filtering and first order texture models in SAR images, *IGARSS '90 Remote Sensing Science for the Nineties (10th Annual International)*, pp2409–2412.

9. Horn, B. K. P. & Schunck, B. G. (1981), Determining Optical Flow. *Art. Intelligence* **17**, pp185–189.